Aerodynamic Noise Simulation and Quadrupole Noise Problem of 600km/h High-Speed Train

XIAOMING TAN[1], TIANTIAN WANG [1,2], BOSEN QIAN[2], BIN QIN[2], AND YIBIN LU[2]

[1]College of Mechanical and Vehicle Engineering, Hunan University, Changsha 410082, China
[2]Key Laboratory of Traffic Safety on Track, Ministry of Education, School of Traffic and Transportation Engineering, Central South University, Changsha 410075, China

Corresponding author: Tiantian Wang (wangtt@hnu.edu.cn)

ABSTRACT The quadrupole aerodynamic noise is a difficult problem in numerical simulation of the aerodynamic noise. The Kirchhoff-Ffowcs Williams and Hawkings (K-FWH) equation method and the three-dimensional compressible Large Eddy Simulation (LES) method are adopted in this manuscript for aerodynamic noise accuracy simulation of 600km/h high-speed train. The influence of different distributions of penetrable integral surfaces on the results of far-field aerodynamic noise is discussed. The optimum combination form of penetrable integral surfaces is obtained. The aerodynamic noise of high-speed train considering quadrupole can be calculated efficiently and accurately by using the upstream body surface and wake area penetrable integral surface as sound source surface. The wake area penetrable integral surface should contain the main vorticity structure of the wake as far as possible and the surface vorticity amplitude should be insignificant. The contribution rate of the dipole and quadrupole to the total aerodynamic noise energy of high-speed train is different. The aerodynamic noise energy of the upstream measurement points is mainly dipole aerodynamic noise energy, while that of the downstream measurement points is mainly dipole and quadrupole noise energy. The method proposed in this manuscript is of great significance in the aerodynamic noise numerical simulation of 600km/h high-speed train.

INDEX TERMS 600km/h high-speed train, quadrupole noise, large eddy simulation, aerodynamic noise, penetrable integral surface method.

I. INTRODUCTION

New technologies applied to China's high-speed trains allows operational speeds up to 400 km/h, which up to 600 km/h are foreseen in the near future with the current research ongoing. However, the aerodynamic noise becomes one of the main limitations and challenges with the increase of running speed. When the speed of high-speed train is less than 350 km/h, the dipole aerodynamic noise is the main noise source, and the quadrupole aerodynamic noise can be neglected [1]–[11]. When the running speed of high-speed train is increased to 600 km/h (the corresponding Mach number is about 0.49), the impact effect in the windward zone, the separation flow strength in the streamlined shoulder zone of the head/tail car, the overflow strength on both sides of the bogie cabin and the mixing effect in the tail flow zone will become stronger. The quadrupole aerodynamic noise is produced when turbulent

The associate editor coordinating the review of this article and approving it for publication was Rosario Pecora.

masses in space friction with each other or within themselves. It is generally believed that the quadrupole aerodynamic noise cannot be ignored when the incoming Mach number is greater than 0.3. As a result, the quadrupole noise around high-speed train becomes stronger, which makes the aerodynamic noise problem of high-speed train more complex.

Compared with the theoretical and experimental research, numerical simulation has the advantages of the short research cycle, low cost and abundant flow/sound field information, which becomes one of the main research methods. Quadrupole aerodynamic noise numerical simulation technology is widely used in aerospace engineering, but it is seldom used in the field of high-speed train. The technology for high-speed train is different from that for aerospace engineering due to the large slenderness ratio and ground effect.

The numerical simulation methods of aerodynamic noise can be divided into two categories: direct and indirect numerical simulation method [12], [13]. Direct numerical simulation method is to solve the Navier-Stokes equation, the linear

Euler equation or the acoustic disturbance equation directly, which does not rely on the acoustic model. The coupling relationship between vortices and potential flow, the formation of acoustic energy flow, the energy conversion in flow field and the sound production mechanism in airflow can be investigated based on the method [14]–[16]. This method requires refinement of the grid distribution to the level of dissipative scale, discrete format with low dissipation, low dispersion and high accuracy and appropriate acoustic non-reflective boundary conditions [17]–[19]. As a result, this method is limited in numerical simulation of engineering applications, such as the aerodynamic noise problem of high-speed train [20], [21].

The theoretical basis of the indirect numerical simulation method is Lighthill's acoustic analogy theory. The theory is a ''black box'' theory, which needs to know the flow-induced sound source in advance. The flow/sound field equation are artificially decoupled and the flow/sound field solutions are obtained by experimental or numerical methods. The method is widely used in engineering application, which is the main method for the aerodynamic noise simulation of high-speed train [1]–[11].

According to the classical FW-H equation method [22], the calculation of the quadrupole aerodynamic noise should not only accurately simulate the Lighthill stress caused by the friction between turbulent masses or the internal friction of turbulent masses in the surrounding space of high-speed trains, but also integrate the Lighthill stress in space. For the Lighthill stress accurate simulation, the generation, development and dissipation of turbulent masses in space are needed to capture in the flow field simulation, which leads to very stringent requirements on the turbulence model, computational grid, and discrete format of flow field simulation. The Lighthill stress volume integration process is relatively easy to implement for small-scale grids,, but difficult for large-scale grids. It makes the simulation of the high-speed train quadrupole aerodynamic noise quite difficult and no published literature has successfully predicted the high-speed train quadrupole aerodynamic noise.

The K-FWH equation method can establish the sound source integration surface in the vicinity of high-speed trains [23]. The radiated noise from the penetrable integral surface includes the dipole noise on the body surface and the quadrupole noise in the space area between the body and the penetrable integral surface. The method is widely used in the aerodynamic noise simulation of the helicopter propeller [24]–[26], the aircraft wing [27], [28] and the jet flow [29]–[31]. Because the process of sound waves propagation in space cannot be simulated based on incompressible gas method, the coupling effect between the flow field and the sound field cannot be simulated. As a result, the K-FWH equation method and the three-dimensional compressible Large Eddy Simulation (LES) method are adopted in this manuscript for the aerodynamic noise accuracy simulation of 600km/h high-speed train. The influence of penetrable integral surfaces at different positions on the simulation

results of far-field aerodynamic noise is discussed and the reasonable position/combination form of the penetrable integral surface are determined. The quadrupole noise problem of 600km/h high-speed train is analyzed and a series of corresponding conclusions are obtained. The method proposed in this manuscript is of great significance in the aerodynamic noise numerical simulation of 600km/h high-speed train.

II. MATHEMATICAL-PHYSICAL MODEL
A. LARGE EDDY SIMULATION METHOD
The LES method has a good ability of capturing eddy and flow field fluctuation, which is suitable for the refined flow field simulation. The method is adopted in this manuscript and the detailed information about the method can be found in reference [32]–[35].

B. K-FWH EQUATION
Based on the traditional FW-H equation[22], Francescantonio [23] derives the K-FWH equation with a wider application range by using the basic idea of Kirchhoff method [36]:

$$\frac{1}{c_0^2}\frac{\partial^2 p_{sound}}{\partial t^2} - \nabla^2 p_{sound} = \frac{\partial^2}{\partial x_i \partial x_j}\left\{T_{ij}H(f)\right\}$$
$$- \frac{\partial}{\partial x_i}\left\{[p_{ij}n_j + \rho u_i(u_n - v_n)]\delta(f)\right\}$$
$$+ \frac{\partial}{\partial t}\left\{[\rho_0 u_n + \rho(u_n - v_n)]\delta(f)\right\} \tag{1}$$

where p_{sound} is the sound pressure, t is the time, p_{ij} is the fluid stress tensor, ρ is the fluid density, c is the sound velocity, u is the airflow velocity, v is the moving velocity of sound source, $\delta(f)$ and $H(f)$ represent Dirac trigonometric function and Heaviside function, respectively. The subscripts i and j are minor scales. The subscripts n is the surface direction vector. The subscripts 0 represents the far filed. It represents sound source plane when $f = 0$. The $T_{ij} = \rho u_i u_j + \left[p - c0^2(\rho - \rho0)\right]\delta_{ij} - \tau_{ij}$ represents Lighthill stress tensor.

The far-field solution of K-FWH differential equations can be obtained by using free space Green's function and generalized function theory [37], [38]. The quadrupole noise model is shown below:

$$4\pi p_{sound,Q}(\vec{x},t)$$
$$= \int_{f>0}\left(\frac{K_1}{c_0^2 r} + \frac{K_2}{c_0 r^2} + \frac{K_3}{r^3}\right)dV\Bigg|_{ret}$$
$$K_1 = \frac{T_{rr}''}{(1-M_r)^3} + \frac{M_r''T_{rr} + 3M_r'T_{rr}'}{(1-M_r)^4} + \frac{3M_r'^2 T_{rr}}{(1-M_r)^5}$$
$$K_2 = \frac{-T_{ii}''}{(1-M_r)^2} - \frac{4T_{M_r}' + 2T_{M_r'} + M_r'T_{ii}}{(1-M_r)^3}$$
$$+ \frac{3[(1-M^2)T_{rr}' - 2M_r'T_{M_r} - M_iM_i'T_{rr}]}{(1-M_r)^4}$$
$$+ \frac{6M_r'(1-M^2)T_{rr}}{(1-M_r)^5}$$

$$K_3 = \frac{2T_{MM} - (1 - M^2)T_{ii}}{(1 - M_r)^3} - \frac{6(1 - M^2)T_{M_r}}{(1 - M_r)^4}$$
$$+ \frac{3(1 - M^2)^2 T_{rr}}{(1 - M_r)^5}$$

$$T_{MM} = T_{ij}M_iM_j; \quad T_{M_r} = T_{ij}M_i\hat{r}_j; \quad T_{M'_r} = T_{ij}M'_i\hat{r}_j;$$
$$T'_{M_r} = T'_{ij}M_i\hat{r}_j; \quad T''_{rr} = T''_{ij}\hat{r}_i\hat{r}_j; \quad M_r = M_i\hat{r}_i; \quad M'_r = M'_i\hat{r}_i$$

$$(2)$$

where M represents the Mach number vector of the body source in the solid surface reference system. The "'" and "''" represent the 1st and 2nd order time derivative, respectively. The "ret" represents delay time item. $T_{rr} = T_{ij}\hat{r}_i\hat{r}_j$ represents two shrinkage of Lighthill stress tensor. The r represents the unit radiation radial vector.

The dipole noise model is shown below:

$$4\pi p_{sound,L}(\vec{x}, t)$$
$$= \frac{1}{c_0} \int_{f=0} \left[\frac{L'_r}{r(1 - M_r)^2} \right]_{ret} ds + \int_{f=0} \left[\frac{L_r - L_M}{r^2(1 - M_r)^2} \right]_{ret} ds$$
$$+ \frac{1}{c_0} \int_{f=0} \left\{ \frac{L_r \left[rM'_r + c_0(M_r - M^2) \right]}{r^2(1 - M_r)^3} \right\}_{ret} ds$$

$$L_r = L_i\hat{r}_i; \quad L'_r = L'_i\hat{r}_i; \quad L_M = L_iM_i; \quad L_r = L_i\hat{r}_i$$
$$L_i = p_{ij}n_j + \rho u_i(u_n - v_n) \quad (3)$$

The monopole noise model is shown below:

$$4\pi p_{sound,T}(\vec{x}, t)$$
$$= \int_{f=0} \left[\frac{\rho_0(U'_n + U_{n'})}{r(1 - M_r)^2} \right]_{ret} ds$$
$$+ \int_{f=0} \left\{ \frac{\rho_0 U_n \left[rM'_r + c_0(M_r - M^2) \right]}{r^2(1 - M_r)^3} \right\}_{ret} ds$$

$$U_n = U_i\hat{n}_i; \quad U_{n'} = U_i\hat{n}'_i; \quad U'_n = U'_i\hat{n}_i$$
$$U_i = \frac{\rho u_i}{\rho_0} + \left(1 - \frac{\rho}{\rho_0} \right) v_i \quad (4)$$

When the sound source surface is a solid surface in the flow field, the $p_{sound,L}(\vec{x}, t)$ and $p_{sound,T}(\vec{x}, t)$ are both the surface integral on the solid surface, and represents the noise radiated by the dipole noise source and the monopole noise source, respectively. The $p_{sound,Q}(\vec{x}, t)$ is the volume integral of the whole computational domain, and represents the noise radiated by the quadrupole aerodynamic noise source. When the sound source surface is a penetrable integration surface that deviates from the solid surface, the $p_{sound,L}(\vec{x}, t)$ and $p_{sound,T}(\vec{x}, t)$ are the surface integral on a permeable integral surface and their sum represents the total noise radiated by the solid surface monopole noise source, the solid surface dipole noise source and the quadrupole aerodynamic noise source between the solid surface and the integrable surfaces. The $p_{sound,Q}(\vec{x}, t)$ is the volume integral of the calculation domain outside the penetrable integration surface.

III. NUMERICAL SIMULATION MODEL

The geometric model shown in Fig. 1 is a high-speed train with three cars, with bogies and without pantographs at a
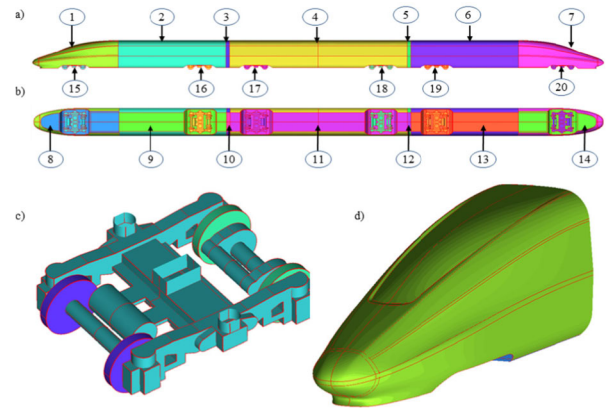

FIGURE 1. Geometric structure of the high-speed train: (a) side view, (b) bottom view, (c) bogie, and (d) the streamlined part. The list of components in the figure is as follows. 1: The upper part of the head car's streamlined part; 2: The upper part of the head car's carriage; 3: The upper part of the intercoach windshield 1; 4: The upper part of the mid-car; 5: The upper part of the intercoach windshield 2; 6: The upper part of the tail car's carriage; 7: The upper part of the tail car's streamlined part; 8: The bottom of the head car's streamlined part; 9: The bottom of the head car's carriage; 10: The bottom of the intercoach windshield 1; 11: The bottom of the mid-car; 12: The bottom of the intercoach windshield 2; 13: The bottom of the tail car's carriage; 14: The upper part of the head car's streamlined part; 15: bogie 1; 16: bogie 2; 17: bogie 3; 18: bogie 4; 19: bogie 5; and 20: bogie 6.
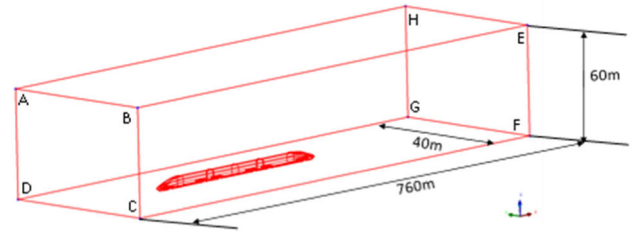

FIGURE 2. Calculational domain.

scale of 1:8. The full-size model has a length of 79.6 m, a height of 4.08 m, and a width of 3.36 m. Fig. 2 shows the calculational domain, which is 760m, 60m and 40m at x, y and z direction, respectively. Because the Reynolds number of the calculation model is 5.5×10^6 and the Reynolds number is located in the second self-model area of the train, it shows that the flow field of the scaled model in this study is similar to that of the full-scale model. Thus, the scaled model can be used in this study.

The surface ABCD is set as pressure far field boundary. The surface EFGH is set as pressure outlet boundary. The both sides and top surface are set as symmetric boundary. The surface of the train model is set as a non-slip boundary condition with a velocity of 0. The ground is set as a sliding boundary condition with the inflow velocity. The air is set as ideal gas and the viscosity is calculated based on the Sutherland formula [39].

The computational mesh in this study is developed from the basis of the grid of the reference [32], so that it can match the aerodynamic noise simulation requirements of 600km/h high-speed train. The computational mesh is
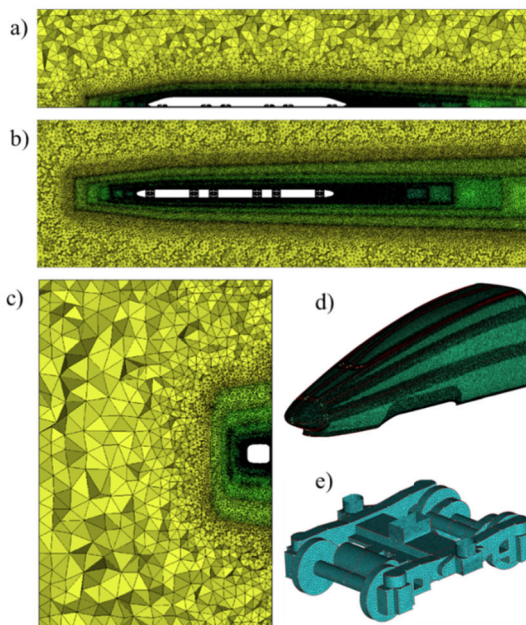
FIGURE 3. Calculational domain Mesh distribution: (a) longitudinal plane; (b) x-y plane of the train nose; (c) cross section of the streamlined shoulder; (d) streamlined part; (e) bogie.
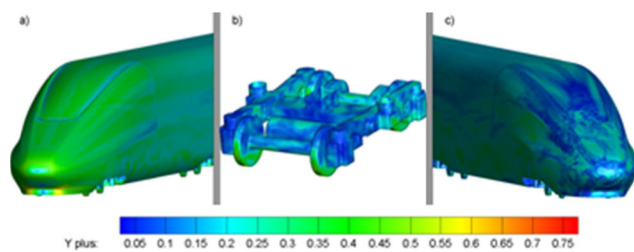

FIGURE 4. Y-plus distribution (free flow speed: 97.22 m/s): (a) head car; (b) first bogie; (c) tail car.

shown in Fig. 3 and the total number of the body meshes is about 260 million.

Appropriate boundary layer grid distribution and spatial grid distribution are two basic requirements for grid distribution in high precision LES. Boundary layer mesh distribution strategy in reference [32] is adopted for grid generation in this manuscript and the Y-plus distribution is shown in Fig. 4. The ratio of mesh scale to local integral scale (l_{Δ}/l_t) is selected as spatial mesh distribution parameters and the distribution is shown in Fig. 5.

It can be observed from Fig. 4 and Fig. 5 that, the Y-plus of the train body surface and the l_{Δ}/l_t of the most spatial mesh are less than 1. As a result, mesh in this manuscript can meet the requirements of accurate calculation of large eddy model.

The numerical simulations of 600km/h high-speed train are conducted using ANSYS Fluent, which is a finite volume method based solver. For steady flow field calculation, explicit pressure basis solution method and the SST k-ω turbulence model are selected. The common simple algorithm is selected for the coupling of pressure and velocity.
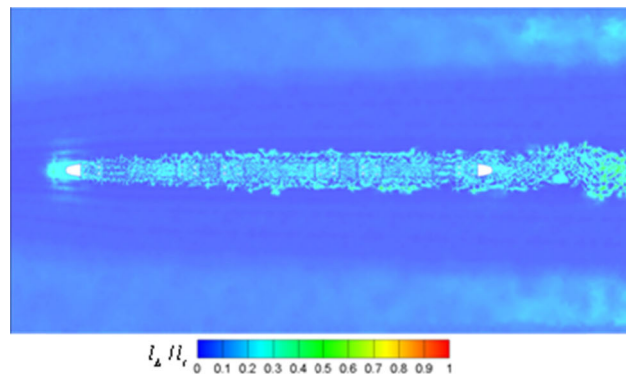

FIGURE 5. l_{Δ}/lt distribution (free flow speed: 97.22 m/s).

The standard discretization scheme is selected for the pressure terms in the governing equations. The convection term is discretized using Second Order Up Wind scheme. The steady flow field selected as the basis flow field and the LES method is selected for unsteady flow field calculation. The Smagorinsky model is selected for the Subgrid model. The couple algorithm is selected for the coupling of pressure and velocity. The calculation time step is set as 5e-5s and 35 steps are iterated in each time step. The total number of the calculation time step is 10000. The numerical simulation method in this manuscript has been verified in reference [32].

IV. SELECTION OF PENETRABLE INTEGRAL SURFACE

Theoretically, penetrable integral surface of the K-FWH equation can be established anywhere in the computational domain[40]. The acoustic radiation calculation results of penetrable integral surfaces located in the different regions or different shapes in engineering practical applications are quite different [41], [42]. As a result, the selection of penetrable integral surface is one of the keys to the refined aerodynamic noise simulation of 600km/h high-speed train.

Considering that the high-speed train head/tail car has a streamlined shape, the cross-sectional shape of the boundary layer exhibits the characteristics of "upper narrow and lower wide", the thickness of the boundary layer is thicker toward the downstream, the width of the disturbance zone is wider toward the downstream, the length of the wake of the high-speed train is larger than that of the upstream zone, and the mesh amount is reduced. The shape of the penetrating integral face is composed of three prisms, as shown in Fig. 6. The part I includes the streamlined part of the head car and the appropriate upstream area. The part II includes all three cars without the streamlined parts of the head and tail car. The part III includes the streamlined part of the tail car and the appropriate downstream area. The cross-sectional shape of the three prisms is characterized by "upper narrow and lower wide", and the width value and height value from the top of the train are larger downstream; the top of the first and third prisms are close to the streamline position of the head/tail car, respectively, and the length of the downstream area of the envelope of the third prism is longer than that of the upstream

TABLE 1. The dimensions of the five penetrable integral surface (m).

	a1	a2	a3	a4	a5	b1	b2	b3	b4
Surface 1	5.0	12.0	56.6	12.0	40.0	2.1	0.3	0.5	2.0
Surface 2	10.0	12.0	56.6	12.0	50.0	2.2	1.2	1.8	2.5
Surface 3	15.0	12.0	56.6	12.0	70.0	2.7	2.3	3.0	3.0
Surface 4	20.0	12.0	56.6	12.0	100.0	3.2	3.6	4.4	3.5
Surface 5	25.0	12.0	56.6	12.0	140.0	3.8	5.2	6.1	6.2

TABLE 2. The combination cases of the penetrable integral surface.

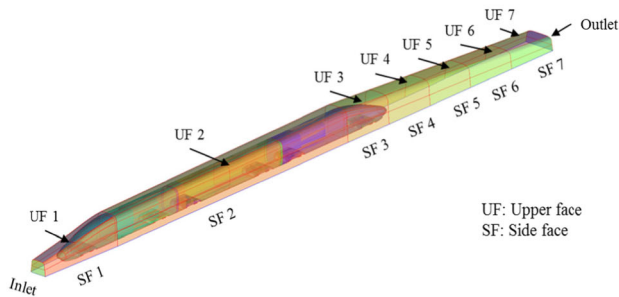| Case	Combination form
1	Inlet/Outlet; UF 1-7; SF 1-7
2	UF 1-7; SF 1-7
3	Inlet/Outlet; UF 1, 3-7; SF 1, 3-7; the streamlined shoulder zone of the head/tail car
4	UF 1, 3-7; SF 1, 3-7; the streamlined shoulder zone of the head/tail car
5	UF 1-6; SF 1-6
6	UF 1-5; SF 1-5
7	UF 1-4; SF 1-4

FIGURE 6. The shape of the penetrable integral surface.

FIGURE 7. Dimensional drawing of penetrable integral surface.
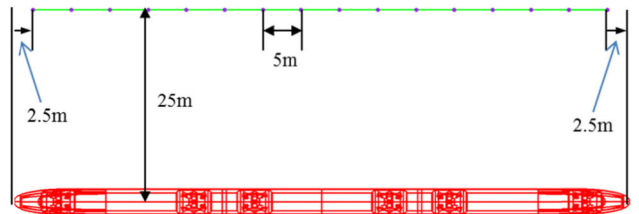
FIGURE 8. Dimensional drawing of the measurement points distribution along the train length direction.

area of the envelope of the third prism. The definitions of the penetrable integral surfaces are shown in Fig. 6.

In order to study the influence of the penetrable integral surface distribution on the simulation results of 600km/h aerodynamic noise, five nested penetrable integral surfaces are established. The five surfaces from the inside to the outside are named as the surface 1 to surface 5. The definitions of the penetrable integral surface dimensions are shown in Fig. 7. The shapes of the surfaces are similar and the dimensions of each surface are listed in Table 1., Seven combination cases of the penetrable integral surface are investigated to study the influence of the penetrable integral surface. The combination form of each case is shown in Table 2.

For investigating the radiated noise of trains, 16 measurement points are set every 5m along the train length direction, which is 25 meters from the track axis and 3.5 meters from the ground. The dimensional drawing of the measurement
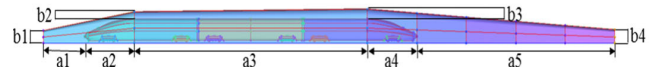
points distribution is shown in Fig. 8. In order to consider the ground reflection, according to the principle of mirror reflection, 16 measurement points symmetrical to the above 16 points are arranged. Symmetrical surface is the ground. The calculation process of radiated noise can be seen in reference [1].

In order to clarify the influence of the position of the penetrable integral surface on the aerodynamic noise results of high-speed trains in the far field, the A-weighted sound pressure levels of the case 1 of the penetrable integral surface 1-5 are calculated by K-FWH equation at 16 measurement points. The ground reflection problem is considered by using the mirror imaging principle and the results are shown in Fig. 9. The noise called "train" is produced by the
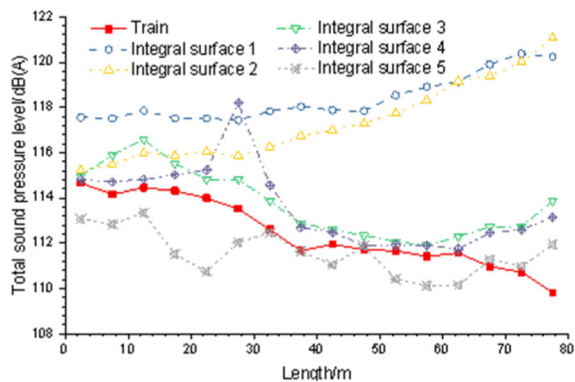
FIGURE 9. A-weighted sound pressure levels of the case 1 of the penetrable integral surface 1-5.
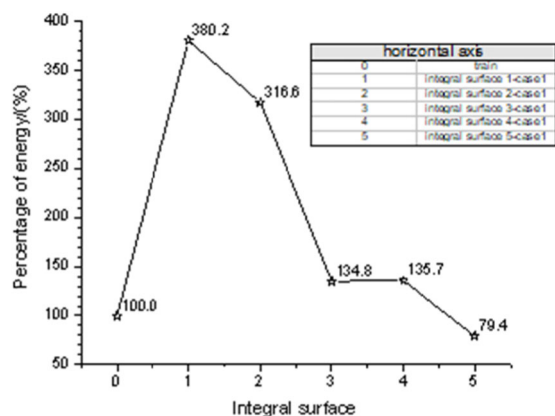

FIGURE 10. The ratio percentages of the total radiation equivalent sound power values of the case 1 of the penetrable integral surface 1-5 and the result of train.

FIGURE 11. Distribution of vorticity amplitude on the penetrable integral surface (unit: 1/s): a) Surface 1; b) Surface 2; c) Surface 3; d) Surface 4; e) Surface 5.

dipole sources distributed on the train surface. These results are also simulated, and have been published in my doctoral dissertation.

As can be seen from Fig. 9, the calculation results of the five penetrable integral surfaces are different, which is consistent with other conclusions [41], [42]. At the measurement point 1-8, the average values of the A-weighted sound pressure level of the penetrable integral surface 1-5 are about 4.0dB(A), 2.3dB(A), 1.2dB(A), 1.3dB(A) and −1.5dB(A) larger than that of high-speed train, respectively. At the measurement point 9-16, the differences are 7.9 dB(A), 7.5 dB(A), 1.3 dB(A), 1.0 dB(A) and −0.3 dB (A), respectively.

In order to further quantify the difference of the calculation results of each penetration integral surface, the percentage of the calculation results of each integral surface (case 1) relative to the calculation results of the train is counted. The results are shown in Fig. 10. The calculation results are the total equivalent sound power of 16 measurement points.

It can be seen from Fig. 10 that the total equivalent sound power radiated by the penetrable integral surface 1-5 at 16 measurement points is 3.80 times, 3.17 times, 1.35 times, 1.36 times and 0.79 times of that of the train, respectively.
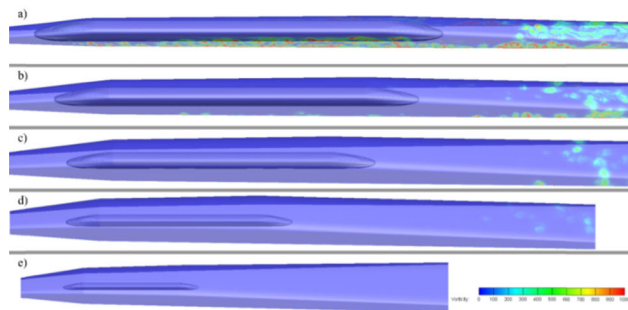
It shows that when the penetrable integral surface is extrapolated from the surface 1 to the surface 3 and the surface 4 to the surface 5, the total equivalent sound power decreases gradually. When the penetrable integral surface is extrapolated from the surface 3 to the surface 4, the total equivalent sound power does not change much.

Fig. 9 and Fig. 10 are due to explain the reason for the variation of the curves. Fig. 11 showes the vorticity magnitude nephogram on five penetrable integral surfaces. As can be seen from the figure, the vorticity magnitude distributions on the upstream and downstream surfaces of the surface 1 and surface 2 are significant. That of the surface 3 is slightly significant and that of the surface 4 and surface 5 are insignificant. It is generally believed that:

1) The fluctuation intensity of the flow field in the region with significant vorticity is obvious, the non-linear effect in the region is obvious. For the penetrable integral surface in this paper, the surface 1 and surface 2 do not contain enough information of sound sources, and there may be significant non-linear effects on the upstream and downstream surfaces of the penetrable integral surface, which makes the K-FWH equation produce pseudo-sound when integrating.

2) The surface may lose part of the vocal region if the penetrable integral surface is too small, which makes the radiated noise results deviate from the correct results.

3) The mesh size of the inner region of the enclosure should be less than 1/6 of the wavelength of the main acoustic wave. In practical applications, it may fail to meet the requirement, resulting in significant numerical dissipation, which makes the result of radiated noise smaller.

Combining with Fig. 10, it can be seen that the equivalent sound power of penetrable integral surface 1 and 2 at 16 measurement points are much larger than that of other surfaces, because the A-weighted sound pressure level radiated by the penetrable integral surface 1 and 2 at downstream measurement points is obviously larger than that radiated by other penetrable integral surfaces. As a result, ,there may be significant pseudo-sounds generated by the penetrable integral surface 1 and 2 at the downstream measurement

points, in which the pseudo-sounds generated by the surface 1 are larger than the surface 2. The pseudo-sounds dominate the total radiation of the penetrable integral surface, while the penetrable integral surface 3-5 do not produce significant pseudo-sounds. This is also the reason why the total equivalent sound power of 16 measurement points decreases gradually when the penetrable integral surface is extrapolated from the surface 1 to the surface 3. The gradual transition from 12.5 mm to 75 mm in the space grid scale from the car body to the surface 5. The grid is equivalent to a filter. If the grid scale is too large, the high-frequency sound will be filtered out. As a result, the reason that the total equivalent sound power decreases when the penetrable integral surface is extrapolated from the surface 4 to the surface 5 may be that the large mesh size brings about significant filtering effect.

The maximum sound pressure level of aerodynamic noise radiated from train surface is 97.6 dB(A) at 350 km/h, and the result is dipole aerodynamic noise. The aerodynamic noise of the monopole, dipole and quadrupole is directly proportional to the fourth, sixth and eighth power of the incoming velocity, respectively. In this manuscript, the aerodynamic noise of monopole is not considered in the simulation. The results of the penetrable integration surface radiation only include the dipole and quadrupole noise. As a result, the maximum sound pressure level range of the penetrable integral surface radiation at 600 km/h can be estimated by formula (8) as [111.8 116.5] dB(A).

$$SPL_{v_1} + 60 \log_{10}\left(\frac{v_2}{v_1}\right) < SPL_{v_2} < SPL_{v_1} + 80 \log_{10}\left(\frac{v_2}{v_1}\right)$$
$$(5)$$

The SPL_{V1} and SPL_{V2} represent sound pressure level of incoming velocity v_1 and v_2, respectively. The v_1 is less than v_2.

According to practical experience and the characteristics of flow field structure distribution of high-speed trains, it is predicted that the quadrupole noise of high-speed trains mainly distributes in the wake region. The sound pressure level of the aerodynamic noise radiated from the penetrable integral surface at the measurement point of the wake region should be significantly higher than that radiated from the train. As a result, it is believed that the results of the aerodynamic noise radiated from penetrable integral surface 3 are reasonable, while that radiated from other surfaces have some defects.

The noise at 16 measurement points under cases in Table 2 of penetrable integral surface 3 is analyzed in order to determine the optimum combination form. Fig. 12 shows the A-weighted sound pressure levels of difference cases of the penetrable integral surface 3.

Case 1 contains more parts named 'inlet' and 'outlet' than case 2 for the penetrable integral surface 3, while the A-weighted sound pressure levels at 16 measurement points of the two cases are almost the same. It can be concluded that the acoustic energy radiated by both ends of the penetrable integral surface is almost neglected compared with other parts. This phenomenon also occurs in the comparison results
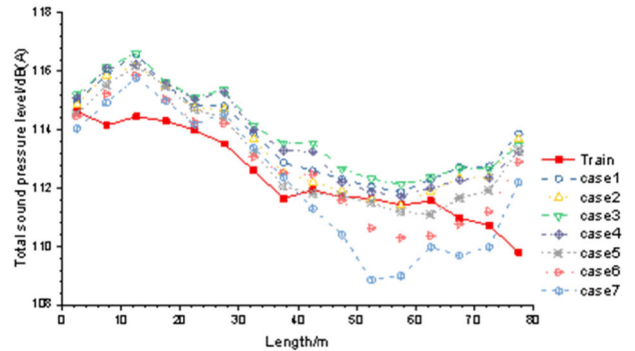

FIGURE 12. A-weighted sound pressure levels of difference cases of the penetrable integral surface 3.

of the A-weighted sound pressure levels of case 3 and 4 of the surface 3.

Comparing with case 1 of the surface 3, case 3 is that the upper 2 and side 2 are replaced by all the train parts between streamlined shoulder of head and tail car. The difference between their sound pressure levels at the measurement point of #1 to #7, #10 to #16 are not more than 0.3 dB (A). Their radiant aerodynamic noise pressure levels at the #8 to #9 measurement points differ by 0.7 dB(A) and 0.9 dB(A), respectively. It shows that the distribution curve of A-weighted sound pressure level predicted by case 1 and case 3 is quite consistent. Compared with case 1, case 3 only needs to refine the grid from the streamline part of the head and tail car to the space area of the penetrable integral surface, which will greatly reduce the grid amount. As a result, the combination form of case 3 has more advantages. This phenomenon also occurs in the comparison results of the A-weighted sound pressure levels of case 2 and 4 of the surface 3.

Comparing with case 1 of the surface 3, case 5, case 6 and case 7 less contains the upper/side 7, upper/side 6-7 and upper/side 5-7, respectively. The sound pressure level radiated by them at all measurement points is less than that of case 2, especially the measurement point near the tail car. The sound pressure level in case 6 and case 7 at the measurement point near the tail car is about 2.5 dB(A) lower than that in case 2. That in case 5 is about 0.6 dB(A) lower than in case 2. This is mainly due to the short length of the wake region contained in case 6 and case 7 and the loss of a part of the vocal region. The distance from the exit of case 5 to the tip of the tail car is about 12 times the height of the train. Therefore, the length of the penetrable integral surface length in the wake area should be larger than 12 times the vehicle height.

As a result, according to the calculation efficiency and prediction accuracy, the best combination form is case 3 or case 4 through the penetrable integral surface 3. The recommended penetrable integral surface length in the wake area should be larger than 12 times the vehicle height.

V. COMPONENT ANALYSIS OF RADIATED NOISE
Equivalent radiation acoustic energy density I is defined as:
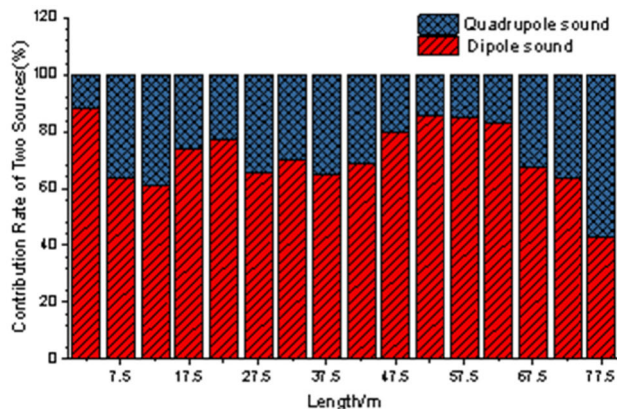
$$I = 10^{SPL/10}$$
$$(6)$$

FIGURE 13. The percentage of aerodynamic noise energy of dipole and quadrupole noise.

The SPL represents the sound pressure level of aerodynamic noise.

Equivalent radiation acoustic energy density of train and penetrable integral surface (the surface 3 of case 3) at these measurement points is calculated by equation (6). The dipole and quadrupole noise are calculated by equation (7). The percentage of aerodynamic noise energy of dipole and quadrupole noise at these measurement points is calculated by equation (8) and (9), respectively. The results are plotted in Fig.13.

$$I_{i,d} = I_{i,train}, \quad I_{i,q} = I_{i,penetrable \ suface} - I_{i,train} \tag{7}$$

$$percentage_{i,d} = I_{i,d} / I_{i,s} \times 100\% \tag{8}$$

$$percentage_{i,q} = I_{i,q} / I_{i,s} \times 100\% \tag{9}$$

where the subscript i denotes the number of the measurement point, $I_{i,d}$ represents dipole source energy at the i-th measuring point, $I_{i,q}$ represents quadrupole source energy at the i-th measuring point, $I_{i,train}$ is the sound energy calculated by the train source at the i-th measuring point, $I_{i,penetrable \ suface}$ is the sound energy calculated by the penetrable integral surface at the i-th measuring point.

It can be seen from Fig. 13, the contribution rate of the dipole and quadrupole aerodynamic noise energy of high-speed train is inconsistent at different measurement points when the incoming velocity is 600 km/h. The contribution rates of the quadrupole aerodynamic noise energy at measurement point 1-15 are in the range of [10%, 40%]. As a result, the dipole aerodynamic noise energy is the main form of aerodynamic noise energy, but the contribution rate of the quadrupole aerodynamic noise energy can not be ignored. At the measurement point 16, the percentage of the dipole and quadrupole aerodynamic noise energy to the total energy is 42.9% and 57.1% respectively. As a result, the aerodynamic noise energy of the dipole and quadrupole noise at the measurement point 16 are both the main form of aerodynamic noise energy.
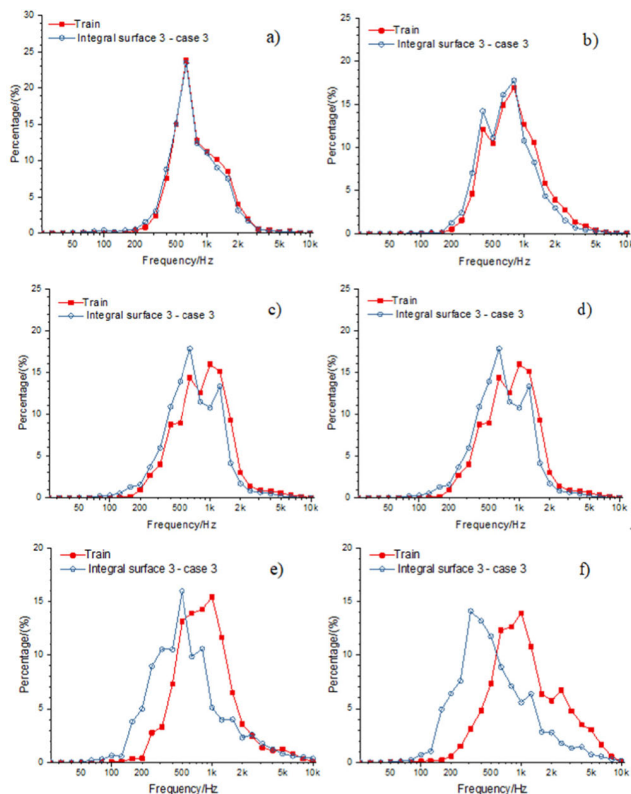

FIGURE 14. The spectrum curves of equivalent radiated acoustic energy density of train and penetrable integral surface at 600 km/h: (a) point 1; (b) point 4; (c) point 7; (d) point 8; (e) point 12; (f) point 16.

In order to discuss the spectrum characteristics of the aerodynamic noise radiated by the trains and penetrable integral surfaces, the spectrum curves of their equivalent acoustic energy density (A-weighted, 1/3 octave frequency range) at 600 km/h at several measurement points are shown in Fig. 14. The analysis frequency range is [25 10k] Hz.

According to Fig. 14, when the inflow velocity is 600 km/h, the coincidence degree of the two spectrum curves is not the same. On the whole, the coincidence degree of the two spectrum curves is poor at the downstream measuring points. In the low frequency range, the spectrum curve of the aerodynamic noise integrated by the train lies above that by the penetrable integral surface, while in high frequency range it is exactly the opposite. This phenomenon also reflects the problem of the high-frequency filtering effect of grids.

According to the spectrum curve at the measuring point 1 shown in Fig. 14 a), in the frequency range below 630 Hz, the result integrated by the train is slightly smaller than that by the penetrable surface, while it is opposite in the frequency range above 630 Hz. The maximum difference between them is less than 1.5%, and they have the same peak frequency of 630 Hz. It shows that the dipole noise energy dominates the total aerodynamic noise energy in the whole frequency range at the measurement point 1.

According to the spectrum curve at the measuring point 16 shown in Fig. 14 f), the main frequency distribution range

of the aerodynamic noise integrated by the train is obviously biased to the high frequency relative to the penetrable surface. The peak frequency of the aerodynamic noise integrated by the train is 1000 Hz, but that by the penetrable surface is 315 Hz. It indicates that the quadrupole aerodynamic noise energy can significantly change the spectral characteristics of the aerodynamic noise and the main frequency distribution range is biased toward the low frequency relative to the dipole noise energy at the measuring point 16,.

As a result, when the incoming velocity is 600 km/h, the contribution rate of the dipole and quadrupole to the total aerodynamic noise energy of high-speed train is different at different positions. The aerodynamic noise energy of the upstream measurement points is mainly dipole aerodynamic noise energy, while that of the downstream measurement points is mainly dipole and quadrupole noise energy. The influence of quadrupole aerodynamic noise on the total aerodynamic noise spectrum is also different. The influence of quadrupole aerodynamic noise at the upstream measurement points on the total aerodynamic noise spectrum is negligible, while at the downstream the quadrupole aerodynamic noise can significantly change the total aerodynamic noise spectrum. The main frequency distribution of quadrupole noise energy tends to be low frequency.

VI. CONCLUSION

The K-FWH equation method and the LES method are adopted in this manuscript for the aerodynamic noise accuracy simulation of 600km/h high-speed train. The influence of different distributions of penetrable integral surfaces on the results of far-field aerodynamic noise is discussed. The optimum combination form of penetrable integral surfaces is obtained. The aerodynamic noise component of the measuring points is analyzed. The following conclusions are obtained.

1) The surfaces of Case 3 for Surface 3 as the sound source surface can efficiently and accurately calculate the aerodynamic noise of high-speed train considering quadrupole noise. The wake penetration integral surface should contain the main vorticity structure of wake as far as possible, and the surface vorticity amplitude should be insignificant, taking into account the spatial grid distribution between the vehicle body and the integral surface.

2) The aerodynamic noise energy of the upstream measurement points is mainly dipole aerodynamic noise energy, while that of the downstream measurement points is mainly dipole and quadrupole noise energy.

3) The influence of quadrupole aerodynamic noise at the upstream measurement points on the total aerodynamic noise spectrum is negligible, while at the downstream the quadrupole aerodynamic noise can significantly change the total aerodynamic noise spectrum.

4) The main frequency distribution of quadrupole noise energy tends to be low frequency compared with dipole noise energy.

REFERENCES

[1] T. Xiao-Ming, Y. Zhi-Gang, T. Xi-Ming, W. Xiao-Long, and Z. Jie, "Vortex structures and aeroacoustic performance of the flow field of the pantograph," *J. Sound Vib.*, vol. 432, pp. 17–32, Oct. 2018.

[2] D. J. Thompson, E. L. Iglesias, X. Liu, J. Zhu, and Z. Hu, "Recent developments in the prediction and control of aerodynamic noise from high-speed trains," *Int. J. Rail Transp.*, vol. 3, no. 3, pp. 119–150, 2015.

[3] H.-H. Yu, J.-C. Li, and H.-Q. Zhang, "On aerodynamic noises radiated by the pantograph system of high-speed trains," *Acta Mechanica Sinica*, vol. 29, no. 3, pp. 399–410, 2013.

[4] Z. Chen, J. Ge, and J. Lin, "Noise and vibration induced by a pantograph of high-speed trains," *J. Acoust. Soc. Amer.*, vol. 131, no. 4, p. 3264, 2012.

[5] S. A. Lee, H. M. Kang, Y. B. Lee, C. W. Kim, and K. H. Kim, "The aeroacoustic analysis for each part of double arm pantograph of high speed train," *J. Comput. Fluids Eng.*, vol. 20, no. 2, pp. 61–66, 2015.

[6] Y. Cao, Y. Bai, and Q. Wang, "Complexity simulation on application of asymmetric bionic cross-section rod in pantographs of high-speed trains," *Complexity*, vol. 8, Aug. 2018, Art. no. 3087312.

[7] J. Su, Y. Sun, and Y. Liu, "Complexity study on the unsteady flow field and aerodynamic noise of high-speed railways on bridges," *Complexity*, vol. 7, Jul. 2018, Art. no. 7162731.

[8] J. Zhang, X. Xiao, D. Wang, Y. Yang, and J. Fan, "Source contribution analysis for exterior noise of a high-speed train: Experiments and simulations," *Shock Vib.*, vol. 12, Dec. 2018, Art. no. 5319460.

[9] C. Mellet, F. Létourneaux, F. Poisson, and C. Talotte, "High speed train noise emission: Latest investigation of the aerodynamic/rolling noise contribution," *J. Sound Vib.*, vol. 293, no. 3, pp. 535–546, 2006.

[10] C. Zhu, H. Hemida, D. Flynn, C. Baker, X. Liang, and D. Zhou, "Numerical simulation of the slipstream and aeroacoustic field around a high-speed train," *Proc. Inst. Mech. Eng., F, J. Rail Rapid Transit*, vol. 231, no. 6, pp. 740–756, 2017.

[11] Y. Zhang, J. Zhang, T. Li, and L. Zhang, "Investigation of the aeroacoustic behavior and aerodynamic noise of a high-speed train pantograph," *Sci. China Technol. Sci.*, vol. 60, no. 4, pp. 561–575, 2017.

[12] M. Wang, J. B. Freund, and S. K. Lele, "Computational prediction of flow-generated sound," *Annu. Rev. Fluid Mech.*, vol. 38, no. 1, pp. 483–512, 2005.

[13] W. Devenport, N. Alexander, S. Glegg, and M. Wang, "The sound of flow over rigid walls," *Annu. Rev. Fluid Mech.*, vol. 50, no. 1, pp. 435–458, 2018.

[14] G. Cunha and S. Redonnet, "On the effective accuracy of spectral-like optimized finite-difference schemes for computational aeroacoustics," *J. Comput. Phys.*, vol. 263, pp. 222–232, Apr. 2014.

[15] S. Zhang, X. Liu, H. Zhang, and C.-W. Shu, "High order and high resolution numerical schemes for computational aeroacoustics and their applications," in *Fluid-Structure-Sound Interactions and Control*. Berlin, Germany: Springer, 2016.

[16] D. R. Hixon, E. Envia, M. D. Dahl, and D. L. Sutliff, "Comparison of computational aeroacoustics prediction of acoustic transmission through a three dimensional stator geometry with experiment," in *Proc. Aerosp. Sci. Meeting*, 2014, p. 1405.

[17] F. Q. Hu, "A perfectly matched layer absorbing boundary condition for linearized euler equations with a non-uniform mean flow," *J. Comput. Phys.*, vol. 208, no. 2, pp. 469–492, 2005.

[18] F. Q. Hu, X. D. Li, and D. K. Lin, "Absorbing boundary conditions for nonlinear Euler and Navier–Stokes equations based on the perfectly matched layer technique," *J. Comput. Phys.*, vol. 227, no. 9, pp. 4398–4424, 2008.

[19] D. K. Lin, X. D. Li, and F. Q. Hu, "Absorbing boundary condition for nonlinear euler equations in primitive variables based on the perfectly matched layer technique," *Comput. Fluids*, vol. 40, no. 1, pp. 333–337, 2011.

[20] C. K. W. Tam, "Computational aeroacoustics: An overview of computational challenges and applications," *Int. J. Comput. Fluid Dyn.*, vol. 18, no. 6, pp. 547–567, 2004.

[21] C. K. W. Tam, *Computational Aeroacoustics: A Wave Number Approach*. Cambridge, U.K.: Cambridge Univ. Press, 2012.

[22] J. E. F. Williams and D. L. Hawkings, "Sound Generation by Turbulence and Surfaces in Arbitrary Motion," *Philos. Trans. Roy. Soc. London A, Math. Phys. Sci.*, vol. 264, no. 1151, pp. 321–342, 1969.

[23] P. di Francescantonio, "A new boundary integral formulation for the prediction of sound radiation," *J. Sound Vib.*, vol. 202, no. 4, pp. 491–509, 1997.

[24] F. Farassat and K. S. Brentner, "Supersonic quadrupole noise theory for high-speed helicopter rotors," *J. Sound Vib.*, vol. 218, no. 3, pp. 481–500, 1998.

[25] V. F. Kopiev, M. Y. Zaytsev, V. I. Vorontsov, S. A. Karabasov, and V. A. Anikin, "Helicopter noise in hover: Computational modelling and experimental validation," *Acoust. Phys.*, vol. 63, no. 6, pp. 686–698, 2017.

[26] Z. Huang, L. Siozos-Rousoulis, T. De Troyer, and D. Ghorbaniasl, "Helicopter rotor noise prediction using a convected FW-H equation in the frequency domain," *Appl. Acoust.*, vol. 140, pp. 122–131, Nov. 2018.

[27] S. Zhong and X. Zhang, "A sound extrapolation method for aeroacoustics far-field prediction in presence of vortical waves," *J. Fluid Mech.*, vol. 820, pp. 424–450, Jun. 2017.

[28] T. Ikeda, S. Enomoto, K. Yamamoto, and K. Amemiya, "Quadrupole corrections for the permeable-surface Ffowcs Williams–Hawkings equation," *AIAA J.*, vol. 55, pp. 2307–2320, 2017.

[29] J. Liu and T. Kagawa, "Computational aeroacoustics simulation of an air micro-injector with dimples shape on the surface of divergent nozzle," *IOP Conf. Ser., Mater. Sci. Eng.*, vol. 249, no. 1, 2017, Art. no. 012009.

[30] V. A. Semiletov, P. G. Yakovlev, S. A. Karabasov, G. A. Faranosov, and V. F. Kopiev, "Jet and jet–wing noise modelling based on the CABARET MILES flow solver and the Ffowcs Williams–Hawkings method," *Int. J. Aeroacoustics*, vol. 15, nos. 6–7, pp. 631–645, 2016.

[31] A. West and M. Caraeni, "Jet Noise Prediction using a Permeable FW-H Solver," in *Proc. 21st AIAA/CEAS Aeroacoustics Conf.*, 2015, p. 2371.

[32] X.-M. Tan, H.-F. Liu, Z.-G. Yang, J. Zhang, Z.-G. Wang, and Y.-W. Wu, "Characteristics and mechanism analysis of aerodynamic noise sources for high-speed train in tunnel," *Complexity*, vol. 12, Dec. 2018, Art. no. 5858415.

[33] A. Favre, "Equations des gaz turbulents compressibles, II. Méthode des vitesses moyennes: Méthode des vitesses macroscopiques pondérées par la masse volumique," *J. Mecanique*, vol. 4, no. 4, pp. 391–400, 1965.

[34] L. D. Mare and W. P. Jones, "LES of turbulent flow past a swept fence," *Int. J. Heat Fluid Flow*, vol. 24, no. 4, pp. 606–615, 2003.

[35] O. V. Vasilyev, T. S. Lund, and P. Moin, "A general class of commutative filters for LES in complex geometries," *J. Comput. Phys.*, vol. 146, no. 1, pp. 82–104, 2001.

[36] G. Kirchhoff, "Zurtheorie der lichtstrahlen," *Annalen Physik*, vol. 254, no. 4, pp. 663–695, 1883.

[37] F. Farassat, "Linear acoustic formulas for calculation of rotating blade noise," *AIAA J.*, vol. 19, no. 19, pp. 1122–1130, 1981.

[38] K. Brentner, "Numerical algorithms for acoustic integrals—The devil is in the details," in *Proc. Aeroacoustics Conf.*, 1996, p. 1706.

[39] J. Vierendeels, B. Merci, and E. Dick, "Benchmark solutions for the natural convective heat transfer problem in a square cavity with large horizontal temperature differences," *Int. J. Numer. Methods Heat Fluid Flow*, vol. 13, no. 8, pp. 1057–1078, 2003.

[40] B. A. Singer, K. S. Brentner, D. P. Lockard, and G. M. Lilley, "Simulation of acoustic scattering from a trailing edge," in *Proc. AIAA*, 1999, p. 231.

[41] W.-S. Choi, Y. Choi, S.-Y. Hong, J.-H. Song, H.-W. Kwon, and C.-M. Jung, "Turbulence-induced noise of a submerged cylinder using a permeable FW–H method," *Int. J. Naval Archit. Ocean Eng.*, vol. 8, no. 3, pp. 235–242, 2016.

[42] M. Wang, S. K. Lele, and P. Moin, "Computation of quadrupole noise using acoustic analogy," *AIAA J.*, vol. 34, no. 11, pp. 2247–2254, 1996.

XIAOMING TAN received the master's and Ph.D. degrees from the School of Traffic and Transportation Engineering, Central South University, Changsha, China, in 2012 and 2019, respectively. He is currently a Candidate of Lecturer with Hunan University. His current research interests include refined flow field and aerodynamic noise of train.

TIANTIAN WANG received the bachelor's and Ph.D. degrees from Beihang University, Beijing, China, in 2012 and 2018, respectively. He is currently a Vice Professor with Central South University and Hunan University. His current research interests include vehicle aerodynamics and vehicle structure, especially train/tunnel aerodynamics, and PHM for trains.

BOSEN QIAN received the master's and Ph.D. degrees from the School of Engineering, Temple University, Philadelphia, PA, USA, in 2017 and 2018, respectively. He is currently an Assistant Professor with Central South University. His research interests include thermoelectric materials, heat and mass transfer, and low vacuum heat and mass transfer.

BIN QIN received the master's and Ph.D. degrees from the Harbin Institute of Technology, China, in 2014 and 2018, respectively. He is currently an Assistant Professor with the School of Traffic and Transportation Engineering, Central South University. His research interests include noise, structural vibration, and fluid mechanics related with railway.

YIBIN LU is currently pursuing the master's degree with the School of Traffic and Transportation Engineering, Central South University, Changsha, China. His major is vehicle operation engineering, and his research interest includes vehicle aerodynamics.

● ● ●